Block-structured grids in Lagrangian 3D edge plasma transport simulations

H. Frerichs[a,b,*], D. Reiter[b], Y. Feng[c], D. Harting[b], O. Schmitz[b]

[a] *German Research School for Simulations Sciences GmbH, 52425 Jülich, Germany*
[b] *Institute for Energy Research - Plasma Physics, Forschungszentrum Jülich GmbH, 52425 Jülich, Germany*
[c] *Max-Planck-Institute for Plasma Physics, Greifswald, Germany*

Abstract

Distinct from conventional Eulerian 2D fluid solvers, applied routinely to magnetic fusion edge plasma studies, complex 3D magnetic topologies are currently treated by the geometrically more flexible Lagrangian schemes, supplemented by Monte Carlo procedures for higher order derivatives (dissipative terms due to diffusion processes) and sources. These particle based algorithms are combined with a field line reconstruction techniques for dealing with partially ergodic magnetic fields, involving field aligned regular grids. A generalization to block-structured grids is carried out, which greatly enhances the range of applicability of present 3D fusion plasma edge codes, in particular also to poloidally magnetic diverted configurations, as envisaged currently for the largest magnetic fusion device under construction: ITER.

Key words: 3D edge plasma transport, Lagrangian method, Coupled CFD-Monte Carlo, Block-structured grids
PACS: 52.65.-y, 52.65.Kj, 52.65.Pp

1. Introduction

Quantification of plasma flows in the domain near exposed surfaces of the plasma container by computer simulations is of key importance, both for guiding interpretation of present fusion experiments and for aiding the ongoing design activities for large future devices such as ITER or the DEMO reactor. There is a large number of computational issues related to the physics of hot, fully ionized and magnetized plasmas near surfaces of the vacuum chamber. In this paper we are concerned with one particular such challenge, namely the numerical quantification of self-consistent kinetic neutral gas and plasma fluid flows in very complex (partially ergodic) magnetic fields, in the absence of any symmetries for plasma and neutral gas dynamics.

Before we discuss the computational aspects, let us briefly introduce the physical problem: Magnetic confinement of thermonuclear plasmas is achieved in toroidal configurations. So called *tokamaks* [1, 2] are one particular magnetic confinement scheme which is currently investigated for the first prototype fusion reactors (See cartoon figure 1 for the essential configurational aspects of the problem). In computational models of those configurations often complete toroidal symmetry is assumed, both for magnetic field, plasma flow, and neutral particle dynamics. This leads to the meanwhile conventional and routinely applied 2D plasma flow (CFD) and plasma surface interaction (kinetic Monte Carlo transport) simulation models (B2-EIRENE [3, 4, 5], EDGE2D-NIMBUS [6, 7], SOLDOR/NEUT2D [8, 9]). An alternative toroidal magnetic confinement concept is the *stellarator* [10], which may in some aspects be regarded as physically simpler (no net plasma current, hence no instabilities related to this non-linear self-confining action), but this is at the expense of a much higher configurational complexity, e.g. magnetic field and particle orbits. In particular the edge plasma region, i.e. the region influenced by plasma contact with the vacuum chamber surfaces, requires at least 3D edge plasma transport models, because the symmetry between plasma transport (largely controlled by the magnetic field $\mathbf{B}$) and the neutral gas cloud formed from plasma neutralization at surfaces, is broken.

Various computational edge plasma transport models for both types of configurations have been developed in the past, which work rather robustly despite the intrinsic complications of all magnetized edge plasma transport models:

- Extremely strong anisotropy (transport time scales parallel and perpendicular to $\mathbf{B}$ differ by 5-6 orders of magnitude).
- High level of non-linearity in parallel transport coefficients: e.g. heat conductivity $\kappa_{\|}$ scales as $T^{5/2}$, heat flux $q_{\|}$ as $T^{7/2}$.
- Wide range of Peclet and Reynolds number within one single simulation, covering incompressible electron- to near sonic ion flows.
- Strong volumetric sources due to plasma recycling at target surfaces. These sources are typically non-local,

*Corresponding author, Email: h.frerichs@grs-sim.de

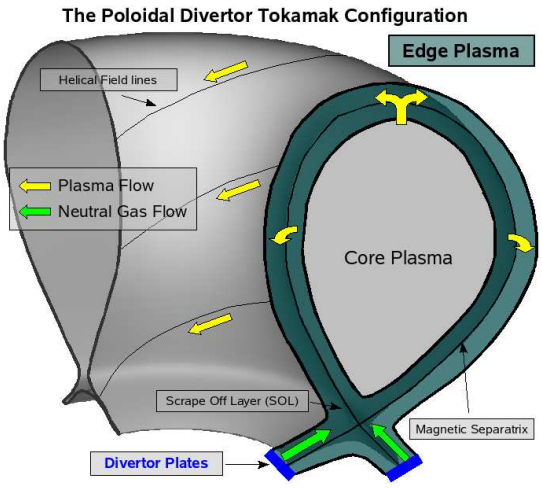

Figure 1: Schematic view of the poloidal divertor tokamak configuration. Directions of plasma and neutral gas flow in the edge plasma region are indicated by colored arrows. The green highlighted region marks the region of interest in edge plasma simulations.

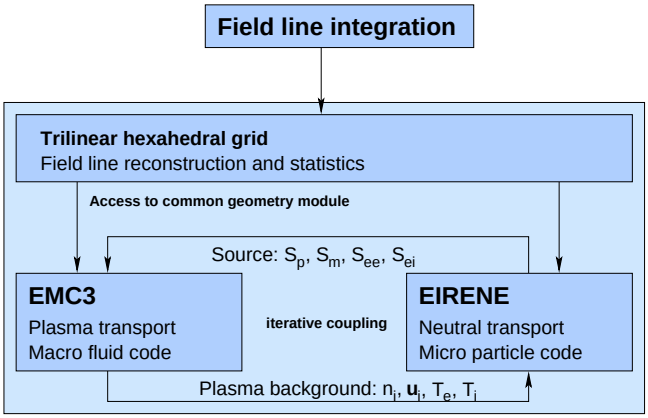

Figure 2: Schematic view of the EMC3-EIRENE code package.

hence require a kinetic (often Monte Carlo) treatment.

For stellarators this combination of a 3D macroscopic (fluid plasma) solver and a 6D (3s3v) microscopic, Monte Carlo (neutral gas) solver is provided by the EMC3-EIRENE code package [11, 12, 13, 4]. Both codes EMC3 and EIRENE are iteratively coupled and share a common geometry module (figure 2).

Also tokamaks may show significant 3D edge plasma effects: e.g. because of

- Resonant magnetic perturbations (RMPs), which create an open chaotic system at the plasma edge, and hence, brake the toroidal symmetry of the confining magnetic field,
- Limiters (local solid apertures introduced into the plasma), breaking the toroidal symmetry of the neutral gas cloud, and hence, of the source terms in the plasma fluid equations), or
- Field line ripple effects resulting from the toroidally discrete set of magnetic field coils.

The EMC3-EIRENE code can be applied to both types of magnetic confinement configurations, e.g. it is currently applied to RMP scenarios at the TEXTOR tokamak [14, 15, 16] and the ITER-startup-limiter configuration [17] as well as the W7-AS [18, 19], W7-X [20] and LHD [21, 22] stellarators (the latter, however, without the divertor region due to issues with the particular field line reconstruction method discussed below).

Because, typically, no strong electric currents flow in the edge region of magnetic fusion devices, in all transport models mentioned the magnetic field $\mathbf{B}$ is externally prescribed, and kept fixed during the entire calculation. The extremely strong anisotropy of parallel to perpendicular (to $\mathbf{B}$) plasma transport does, however, require a precise knowledge of $\mathbf{B}$ at any point and time in the simulation. To keep these two distinct physical processes also separated in the simulation, a local, field aligned coordinate system (with one coordinate line parallel to $\mathbf{B}$) is used. The EMC3-EIRENE code package profits from a very flexible representation of the magnetic field structure, which has already enabled applications to such distinct configurations like the W7-AS stellarator and the ITER-startup-limiter edge. A field line reconstruction technique is used, based upon a computational grid with regular structured toroidal blocks (figure 3), and combined with a reversible field line mapping technique (RFLM) [23] at block boundaries. Such a regular decomposition in the poloidal and radial coordinate, however, is not efficiently applicable to poloidally divertor tokamaks, such as JET, DIII-D, ASDEX-U and ultimately ITER, nor in the complete plasma edge of the LHD stellarator (i.e. including the divertor regionr). The remoteness of the divertor plates from the inner edge plasma boundary (figure 1) would either result at best in a very distorted grid with low resolution in the divertor region, or require the simulation of a much larger, poloidally uniform domain and hence, largely waste computational resources.

In this paper we therefore propose supplementing the RFLM concept with a cell surface mapping technique, which can be implemented in both the Lagrangian CFD part EMC3 and in the kinetic Monte Carlo transport part EIRENE. This allows an arbitrary - but for convenience still block-structured - decomposition of the simulation domain. It is shown that a combination of (a) field line mapping between toroidal blocks and (b) cell surface mapping including the transformation of the local coordinate system at some poloidal or radial cuts allows both accurate magnetic field representations and plasma fluid and neutral gas kinetic transport simulations. This paper is organized as follows:

In the next section we briefly outline the Lagrangian CFD method (combined with Monte Carlo treatment of diffusion) in EMC3 by resorting to the equivalence of the plasma transport equation and a generic Fokker-Planck type equation, and, hence, an underlying stochastic differential equation. Because of the anisotropic transport, the most challenging part is the correct treatment of the sometimes very complex magnetic field structure: closed magnetic flux-surfaces, ergodic layers, magnetic islands and field lines ending on surface elements. In section 3 at first the particular field line reconstruction method implemented in EMC3 is introduced, basically resorting to the work in [23]. This procedure is then generalized towards unstructured grids in the poloidal and radial coordinate to allow for more general grid connectivities. In section 4 numerical tests for this generalization are performed to indicate the correct performance of the generalized code. Finally, in section 5 a typical application of the generalized code to a 3D tokamak edge plasma is presented. We have chosen a model corresponding to a magnetic configuration of the DIII-D tokamak, because this particular tokamak has recently gained large attention due to the success of mitigating certain edge localized instabilities (ELMs [24]) by application of external 3D magnetic perturbation [25], superimposed to the 2D tokamak magnetic field. The main results are summarized in the Conclusions.

2. A Lagrangian scheme for 3D edge plasma transport

Transport processes in magnetized and collisional plasmas, such as the edge plasma in fusion devices, can be described using a fluid approach, the so called Braginskii equations [26]. These are the plasma counterpart to the Navier Stokes equations of conventional fluid dynamics, with similar balance equations for density, momentum and energy. Sources (or sinks) due to interactions with neutral particles are included while an ad hoc ansatz for anomalous cross-field diffusion is applied. We are interested in steady state solutions of these equations (see appendix (41-44)) which are of the generic form

$$\nabla \cdot [\mathcal{V}_{\rm pl}\, \mathcal{F} \,-\, \mathcal{D}_{\rm pl} \cdot \nabla \mathcal{F}] \,=\, \mathcal{S}, \tag{1}$$

for some plasma quantity $\mathcal{F}$ such as electron density n_e or temperature T_e. The pattern of $\mathcal{F}$ is determined by a scalar source $\mathcal{S}$, convection vector $\mathcal{V}_{\rm pl}$ and diffusion tensor $\mathcal{D}_{\rm pl}$. (1) can be transformed into a steady state Fokker-Planck type equation (FPE)

$$\nabla \cdot [\mathcal{V}_{\rm fp}\, \mathcal{F} \,-\, \nabla \cdot \mathcal{D}_{\rm fp}\, \mathcal{F}] \,=\, \mathcal{S}, \tag{2}$$

with corresponding Fokker-Planck drift and diffusion coefficients $\mathcal{V}_{\rm fp}$ and $\mathcal{D}_{\rm fp}$, respectively:

$$\mathcal{V}_{\rm fp} \;=\; \mathcal{V}_{\rm pl} \,+\, \nabla \cdot \mathcal{D}_{\rm pl} \tag{3}$$

$$\mathcal{D}_{\rm fp} \;=\; \mathcal{D}_{\rm pl}. \tag{4}$$

2.1. Lagrangian scheme for FPEs

In order to solver an extremely anisotropic, highly nonlinear Fokker-Planck equation, we apply a Lagrangian scheme, supplemented by a Monte Carlo procedure for diffusion processes and sources. That is, we consider fluid parcels $\Delta\mathcal{F}$ with initial distribution determined by $\mathcal{S}$ and dedicated transition probability $p = p(s, x; t, y)$ for their dynamics. This technique is well known [13] and only a brief description is given here for the context of the present work.

Consider the Ito stochastic differential equation (SDE)

$$dX_t \,=\, a(X_t)\, dt \,+\, b(X_t)\, dW_t, \tag{5}$$

with Wiener process W_t and drift and diffusion coefficients $a(X_t)$ and $b(X_t)$, respectively. It can be shown that the corresponding transition probability p of a Markov process satisfies the Fokker-Planck equation (also known as Kolmogorov forward equation)

$$\frac{\partial p}{\partial t} + \frac{\partial}{\partial y}(ap) - \frac{1}{2}\frac{\partial^2}{\partial y^2}(b^2 p) = 0, \tag{6}$$

if $a(y)$, $b(y)$ are bounded and smooth enough [27]. An approximate solution for the inhomogeneous FPE (2) can be obtained by simulating an ensemble of sample paths, i.e. trajectories of the stochastic process (5), with initial distribution and weight determined by $\mathcal{S}$. An elaborate review of the relation between the probability density and trajectory point of view is e.g. given in [28].

Trajectories are here integrated by using a time discrete approximation $Y_n = Y_{\tau_n}, \tau_n = n\,\tau$ with timestep τ:

$$Y_{n+1} \,=\, Y_n \,+\, a(Y_n)\,\tau \,+\, b(Y_n)\,\Delta W_n, \tag{7}$$

where the initial value Y_0 is sampled from $\mathcal{S}$ and the increments $\Delta W_n = W_{\tau_{n+1}} - W_{\tau_n}$ are independent Gaussian random variables. This is known as the Euler-Maruyama approximation for SDEs [29], in analogy to the Euler approximation for ordinary differential equations. More generally, it can be shown that any transition probabiliy density p with moments

$$\langle \Delta Y \rangle_p \;=\; a(x)\,\tau \tag{8}$$

$$\langle \Delta Y\, \Delta Y \rangle_p \;=\; b^2(x)\,\tau \tag{9}$$

corresponds to a Fokker-Planck equation [30]. So, instead of ΔW_n any random variables R_n with mean and variance

$$E[R_n] \,=\, 0, \qquad E[R_n^2] \,=\, \tau. \tag{10}$$

can be used. In a local, field aligned coordinate system ($\mathbf{e}_\parallel$, $\mathbf{e}_{\perp 1}$, $\mathbf{e}_{\perp 2}$) this scheme can be applied independently for each direction to separate fast parallel from slower perpendicular transport processes. The integration scheme for trajectories in Euler-Maruyama approximation then reads

$$Y^{\parallel}_{n+1} = Y^{\parallel}_{n} + \mathcal{V}^{\parallel}_{\rm fp}\,\tau + \sqrt{2\,\mathcal{D}^{\parallel}_{\rm fp}\,\tau}\,\xi_n \quad (11)$$

$$\mathbf{Y}^{\perp}_{n+1} = \mathbf{Y}^{\perp}_{n} + \mathcal{V}^{\perp}_{\rm fp}\,\tau + \sqrt{4\,\mathcal{D}^{\perp}_{\rm fp}\,\tau}\,\mathbf{b}_{\perp} \quad (12)$$

$$\mathbf{b}_{\perp} = \cos(2\pi\eta_n)\,\mathbf{e}_{\perp 1} + \sin(2\pi\eta_n)\,\mathbf{e}_{\perp 2} \quad (13)$$

with standard Gaussian random variables ξ_n and unit random variables η_n. Because of the application of random numbers, this Lagrangian scheme is often also referred to as Monte Carlo method. Single trajectories of the stochastic process represent sample fluid parcels which are hence referred to as Monte Carlo particles. A track length estimator

$$\mathcal{F}_i = \frac{1}{C_i}\sum_j w_j\,\tau_{ji}, \qquad i = 1,\ldots,N_{\rm cell}, \quad (14)$$

is applied to provide local estimates $\mathcal{F}_i$ in a computational grid (see figure 3) with $N_{\rm cell}$ cells. C_i is the volume of cell i, w_j the weight of MC particle j and τ_{ji} the time it spend in cell i.

2.2. Non-linear transport equations

The method described above provides a solver for given transport coefficients $\mathcal{V}_{\rm fp}$, $\mathcal{D}_{\rm fp}$. These coefficients, however, are functions of plasma parameters, and thus depend on the solution $\mathcal{F}$. In an abstract form, a solver for the linearized version of (2) where $\mathcal{V}_{\rm fp} = \mathcal{V}_{\rm fp}(\mathcal{F}_{\rm in})$, $\mathcal{D}_{\rm fp} = \mathcal{D}_{\rm fp}(\mathcal{F}_{\rm in})$ can be written as a mapping ϕ:

$$\phi : \mathbb{R}^{N_{\rm cell}} \to \mathbb{R}^{N_{\rm cell}}, \mathcal{F}_{\rm in} \mapsto \mathcal{F}_{\rm out}. \quad (15)$$

A self-consistent solution $\mathcal{F}$ of the plasma transport equation is a fixed point $\mathcal{F}^* = \phi(\mathcal{F}^*)$ of the mapping ϕ. Therefore we apply the transport solver ϕ in an iterative procedure. At his point we leave the issue of convergence of noisy fixed point iterations untouched. In practise we consider the relative change of $\mathcal{F}$ between iterations (see section 5.4).

3. Fast reconstruction of magnetic field lines

To avoid time-expensive field line tracing (integration) in the code, a computational grid constructed from toroidal blocks of precalculated magnetic field lines is used (figure 3), and combined with a reversible field line mapping technique (RFLM) at block boundaries. Distinct from the grid for statistics (i.e. for averaging plasma parameters $\mathcal{F}$ over small cells, needed for iteration and graphical output) - which can in principle be arbitrary - the grid for magnetic field line reconstruction requires special attention. The increase in speed of 3-4 order of magnitude with respect to direct field line integration at the position of fluid parcels, however, justifies the additional effort for magnetic grid generation.

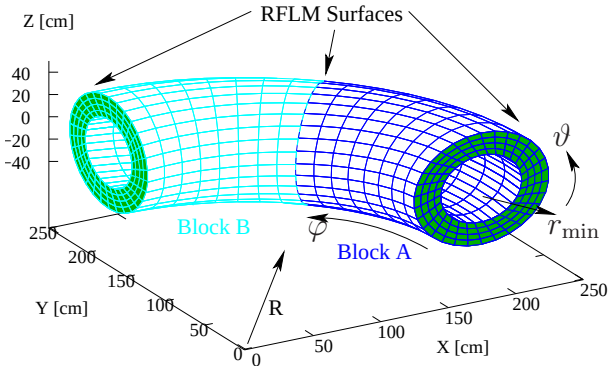

Figure 3: Field aligned grid with 2 toroidal blocks of $\Delta\varphi = 45$ deg each. This kind of grid is used for simulations of the edge plasma at the TEXTOR tokamak in the presence of an RMP field with 4-fold toroidal symmetry.

A field aligned grid is constructed from a set of field lines $\mathbf{x}_i(\varphi) = (R_i(\varphi), Z_i(\varphi))$ for $\varphi \in [\varphi_A, \varphi_B]$ which are calculated in a preprocessing step, using a 5th order Adams-Bashfort scheme with 4 initial Runge-Kutta-Gills backward steps. Grid nodes $\mathbf{x}_{ik}$ are defined as

$$\mathbf{x}_{ik} = \mathbf{x}_i(\varphi_k), \quad \varphi_k = \varphi_0 + k\frac{\Delta\varphi}{2\,N_k}, \quad k = -N_k \ldots N_k, \quad (16)$$

with

$$\varphi_0 = \frac{\varphi_A + \varphi_B}{2}, \quad \Delta\varphi = \varphi_B - \varphi_A. \quad (17)$$

Field lines $\mathbf{x}^*_i$ are then reconstructed by a linear interpolation between nodes:

$$\mathbf{x}^*_i(\varphi) = \varphi^*\,\mathbf{x}_{ik} + (1-\varphi^*)\,\mathbf{x}_{ik+1}, \quad (18)$$

$$\varphi^* = \frac{\varphi - \varphi_k}{\varphi_{k+1} - \varphi_k}, \quad \varphi \in [\varphi_{k+1}, \varphi_k]. \quad (19)$$

Now hexahedral grid cells are defined by a set of 4 of these field lines. Any field line in between is approximated by a bilinear interpolation:

$$\mathbf{x}(\xi,\eta,\varphi) = \sum_{i=1}^{4} \mathbf{x}^*_i(\varphi)\,N_i(\xi,\eta), \qquad \xi,\eta \in [-1,1] \quad (20)$$

of 4 field lines $\mathbf{x}^*_i(\varphi)$, with the shape functions $N_i(\xi,\eta)$ of a 4-node (bilinear) quadrilateral, well-kown in finite element methods (see e.g. [31]). This setup defines a 3D grid with local, field aligned coordinate system, where coordinates lines with $\xi, \eta = \text{const}$ are field line representations.

Multiple toroidal blocks, with a reversible field line mapping [23] between adjacent blocks, are used to allow an accurate representation of partially ergodic fields: At the interface between two adjacent blocks (e.g. between block A and B in figure 3) the relation

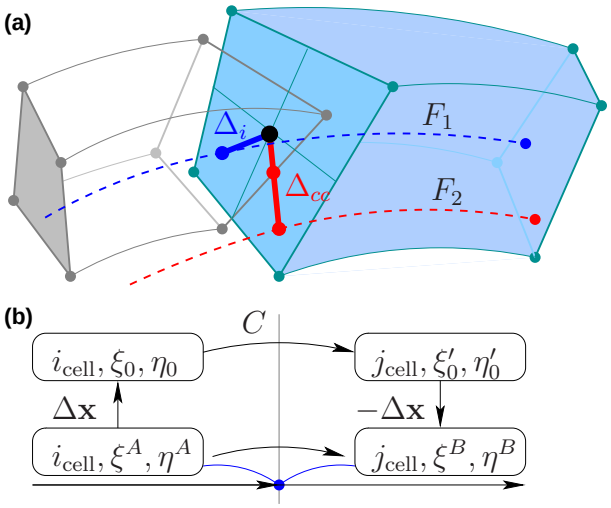

Figure 4: (a) two grid cells at the interface between toroidal blocks and (b) schematic view of the field line mapping technique. Local coordinates for field lines F_1 and F_2 are mapped from the blue cell to the grey cell with a cell mapping (22) at a reference point (black dot) and the correcction *jumps* Δ_i and Δ_{cc}, respectively. In the case of cross-cell *jumps* Δ_{cc}, the *jump* is segmented into two parts, while j_{cell} is updated at the cell boundary and combined with a transformation of local coordinates between cells.

$$\mathbf{x}^{(i_{\text{cell}})}\left(\xi^A, \eta^A\right) = \mathbf{x}^{(j_{\text{cell}})}\left(\xi^B, \eta^B\right) \tag{21}$$

provides with (20) a reversible mapping of field line coordinates. i_{cell} and j_{cell} are cell indices in blocks A and B, respectively, and hence define the set of grid nodes used for interpolation in (20). A similar *multiple local magnetic coordinate system approach* is e.g. used in the 3D heat transport code for edge plasmas E3D [32]. Contrary to the cubic spline interpolation scheme used there, we use a simpler, linear interpolation scheme, which is sufficiently accurate but simple enough to allow calculations of plasma fluid transport (in magnetic coordinates) as well as kinetic neutral transport (in cartesian coordinates) within one single geometry module.

However, when applying the inverse of (20) to obtain the new field line coordinates ξ^B, η^B, the cell number j_{cell} in the adjacent block (i.e. the set of 4 field lines to interpolate from) is not a priori known. This is because of the discontinous cell interface between blocks (figure 4.a). Finding the correct cell number j_{cell} and field line coordinates ξ^B, η^B for a given point $\mathbf{x}$ in a large grid can be quite expensive, however, we can divide this task into two steps: First, in a preprocessing step, a cell mapping C:

$$C : i_{\text{cell}} \rightarrow (j_{\text{cell}}, \xi_0', \eta_0') \tag{22}$$

is defined for one field line (ξ_0, η_0) per cell (e.g. for $\xi_0, \eta_0 = 0$, black dot in figure 4). Once this mapping is defined for all cells at the interface between toroidal blocks, only the displacement

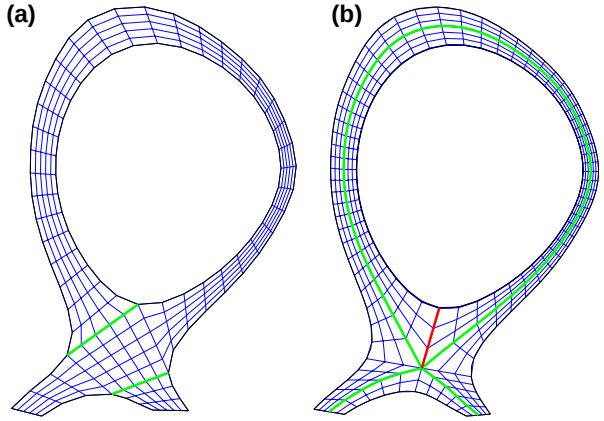

Figure 5: Poloidal cuts of two possible block-structured decompositions of the edge plasma region in a poloidal divertor tokamak configuration. Boundaries of adjacent blocks (green lines) are connected by a cell surface mapping (M_{neigh}, $\mathbf{M}_{\xi\eta}$), red lines indicate periodic cell boundaries.

$$\Delta\mathbf{x} \equiv \mathbf{x}^{(i_{\text{cell}})}(\xi_0, \eta_0) - \mathbf{x}^{(i_{\text{cell}})}\left(\xi^{(z)}, \eta^{(z)}\right), \tag{23}$$

is needed to correct the new coordinates from (22) whenever relation (21) is applied (figure 4.b). Cell internal *jumps* Δ_i can be related to a displacement $(\Delta\xi, \Delta\eta)$ in the new field lines coordinates by (20), so that

$$\left(j_{\text{cell}}, \xi^B, \eta^B\right) = C(i_{\text{cell}}) + (0, \Delta\xi, \Delta\eta)\,. \tag{24}$$

This method gives the exact coordinates (ξ^B, η^B). In the case of cross-cell *jumps* Δ_{cc}, the *jump* is segmented into two parts, while j_{cell} is updated at the cell boundary and combined with a transformation of local coordinates between cells. The details of this depend on the grid topology.

3.1. Structured grids

In structured grids with radial, poloidal and toroidal cell indices $i_r = 0, \ldots, n_r - 1$; $i_p = 0, \ldots, n_p - 1$; $i_t = 0, \ldots, n_t - 1$, this is the simple relation:

$$i_p' = (i_p \pm 1) \mod n_p, \qquad \xi' = \xi, \quad \eta' = \mp 1 \tag{25}$$

$$\text{or} \quad i_r' = i_r \pm 1, \qquad \xi' = \mp 1, \quad \eta' = \eta \tag{26}$$

at poloidal (25) or radial (26) cell surfaces, respectively.

3.2. Unstructured grids

We now turn to unstructured grids, to allow more flexibility in the shape of the simulation domain. This is necessary for simulations of the edge plasma in poloidal divertor tokamaks. Two examples of a block-structured decomposition are shown in figure 5. The field line reconstruction method described above is still applicable in unstructured grids, only (25) and (26) need to be generalized.

In unstructured grids, the grid connectivity is defined by a neighbor relation M_{neigh} between adjacent cells i_{cell}, j_{cell} (see figure 14 for the numbering convention of cell surfaces i_{surf}, i'_{surf}):

$$M_{\text{neigh}} : (i_{\text{cell}}, i_{\text{surf}}) \rightarrow (j_{\text{cell}}, i'_{\text{surf}}), \tag{27}$$

Because of the particular field line reconstruction method, the local field line coordinates need to be transformed as well. For this we need an additional transformation matrix $\mathbf{M}_{\xi\eta}$:

$$(\xi', \eta') = \mathbf{M}_{\xi\eta} \cdot (\xi, \eta), \tag{28}$$

while φ is fixed in the special case when the structure in toroidal direction remains. This transformation matrix depends on the relative orientation of the surfaces i_{surf}, i'_{surf} (see appendix B):

$$\mathbf{M}_{\xi\eta}(i_{\text{surf}}, i'_{\text{surf}}) = (-1)^k \cdot \mathbf{M}_j \tag{29}$$

with

$$\mathbf{M}_0 = \begin{pmatrix} 1 & 0 \\ 0 & -1 \end{pmatrix}, \qquad \mathbf{M}_1 = \begin{pmatrix} 0 & 1 \\ 1 & 0 \end{pmatrix} \tag{30}$$

and integer valued indices k, j:

$$k = \lfloor (i_{\text{surf}} + i'_{\text{surf}})/2 \rfloor, \qquad j = (i_{\text{surf}} + i'_{\text{surf}}) \mod 2.$$

The implementation of the cell surface mapping (M_{neigh}, $\mathbf{M}_{\xi\eta}$) into the EMC3-EIRENE code provides a generalization for simulation domains with arbitrary shape and in particular for poloidal divertor tokamaks. Commonly the simulation domain is divided in an unstructured set of blocks that are connected by (M_{neigh}, $\mathbf{M}_{\xi\eta}$), while a regular structure remains within a block. The remaining part of this paper will demonstrate the correct performance of the generalized code and provide an example for a typical application.

4. Performance tests of the generalized code

The correct performance of the newly implemented cell surface mapping technique in the EMC3-EIRENE code is now briefly demonstrated. For this we consider a well-established simulation scenario for the TEXTOR tokamak with 3D open chaotic system due to RMPs. We introduce an arbitrary 4×4 block decomposition in radial and poloidal direction and re-connect these blocks at the interfaces with a cell surface mapping M_{neigh} (figure 8):

$$M_{\text{neigh}} : (i_b, i_r, i_p, i_t) \rightarrow (i'_b, i'_r, i'_p, i'_t), \tag{31}$$

where i_b is the block number, and i_r, i_p, i_t are radial, poloidal and toroidal cell indices. Local coordinates are transformed according to (28).

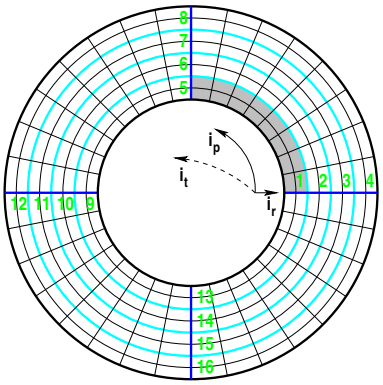

Figure 8: Poloidal cut through a (low resolution) computational grid for TEXTOR with a 4×4 block-structured decomposition. Block boundaries (dark and light blue) are connected by a cell surface mapping for block number i_b (green), cell indices i_r, i_p, i_t and local coordinates ξ, η, τ.

Before performing actual plasma and neutral gas transport calculations, we demonstrate the correct representation of the magnetic field structure. This structure is visualized in figure 6 by means of the wall-to-wall connection length L_c of magnetic field lines. Radial profiles at $\vartheta_1 = 12$ deg and $\vartheta_2 = 34$ deg, as well as poloidal profiles at $r_{\text{min},1} = 42\,\text{cm}$ and $r_{\text{min},2} = 46\,\text{cm}$ are selected. It is shown in figure 6 that they exactly match the reference profiles from a regular structured grid (see figure 3 for definitions of toroidal coordinates $\varphi, \vartheta, r_{\text{min}}$). The physics of such an open chaotic system and its impact on plasma transport is not part of this paper and is investigated elsewhere (e.g. in [33, 34, 35]).

Transport calculation within a 4×4 block decomposition give - as expected - the same results as obtained from a regular grid. This is illustrated in figure 7, again by selected radial and poloidal profiles of the electron temperature T_e and density n_e. The same tests have also been performed for the neutral transport part EIRENE. Hence, these numerical tests exemplify the correct performance of the generalized code.

5. Application to poloidal divertor tokamaks

In this section we like to present the enhanced applicability of the EMC3-EIRENE code. The DIII-D tokamak was chosen as an example for poloidal divertor machines, because of its recent success in ITER relevant research regarding the ELM control issue.

5.1. Computational domain

The selected magnetic configuration is typical for a DIII-D plasma with ITER similar shape (ISS) and $n = 3$ RMP field, i.e. a magnetic field with toroidal C_3 symmetry, and is obtained from the EFIT code [36]. Because of this symmetry, the computational domain may be reduced to one

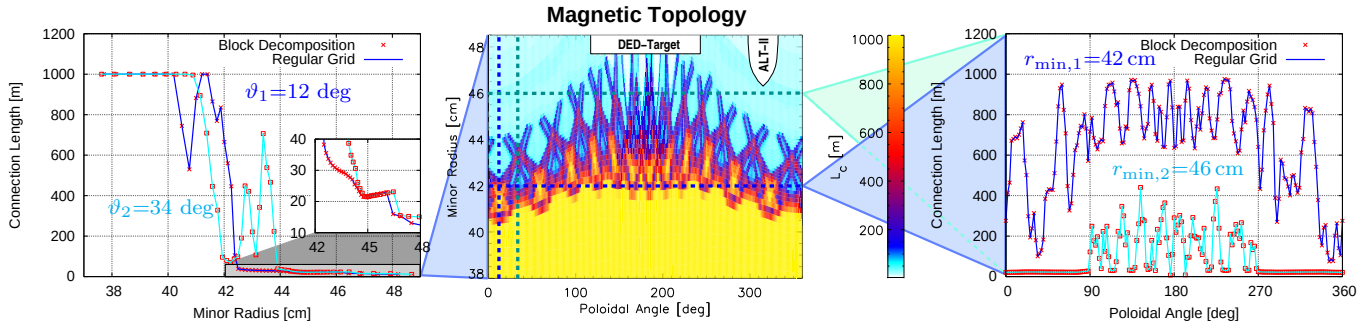

Figure 6: Magnetic Topology of an RMP scenario at the TEXTOR tokamak, depicted by the wall-to-wall connection length L_c of magnetic field lines. The center figure shows a 2D cut at $\varphi = 0$ deg, giving an overview of the magnetic topology. Radial profiles at $\vartheta_1 = 12$ deg and $\vartheta_2 = 34$ deg (left figure) as well as poloidal profiles at $r_{\min,1} = 42\,\mathrm{cm}$ and $r_{\min,2} = 46\,\mathrm{cm}$ (right figure) are selected. Data from calculations within a 4×4 block-structured grid is presented as crosses and boxes, while reference data within a regular grid is presented as solid lines.

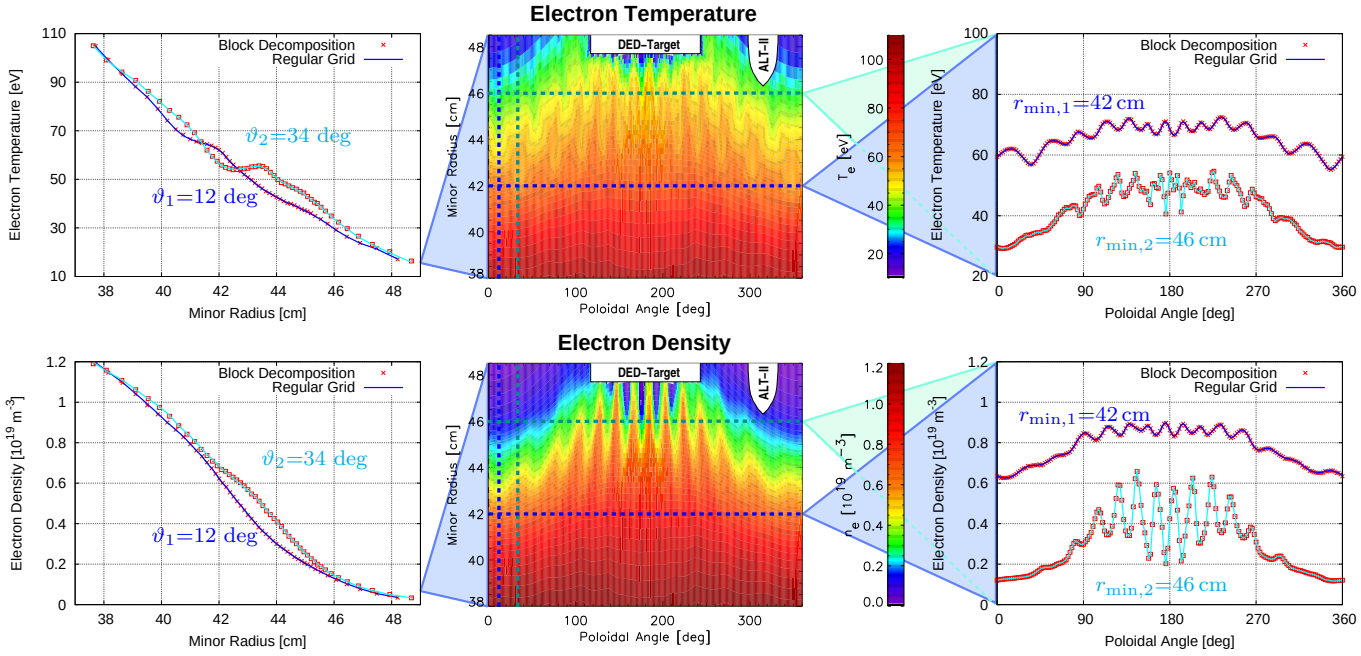

Figure 7: Electron temperature T_e (upper row) and density n_e (lower row) for the magnetic topology from fig. 6. The center column shows 2D cuts at $\varphi = 0$ deg as an overview. Radial profiles at $\vartheta_1 = 12$ deg and $\vartheta_2 = 34$ deg (left column) as well as poloidal profiles at $r_{\min,1} = 42\,\mathrm{cm}$ and $r_{\min,2} = 46\,\mathrm{cm}$ (right column) are selected. Data from calculations within a 4×4 block-structured grid is presented as crosses and boxes, while reference data within a regular grid is presented as solid lines.

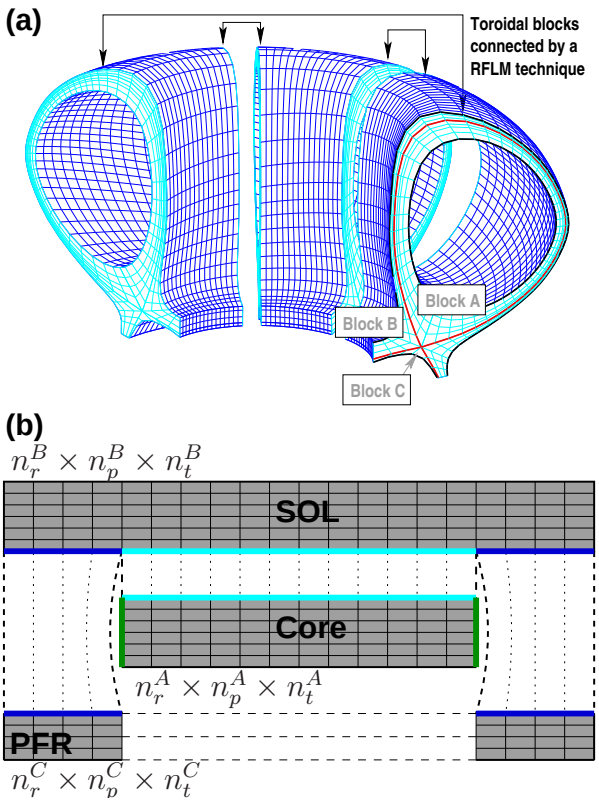

Figure 9: (a) Computational domain for an edge plasma in a poloidal divertor tokamak. The C_3 symmetry in $n = 3$ RMP scenarios allows to reduce the toroidal circumference to $\Delta\varphi = 120$ deg. (b) Topological view of the block-structured decomposition in radial and poloidal direction.

third of the toroidal circumference. A toroidal decomposition into three blocks of $\Delta\varphi = 40$ deg is used (figure 9 a), which is similar to the block size in simulations for TEXTOR, however accounting for the present C_3 symmetry. A further decomposition into three sub-blocks is introduced for each toroidal block to allow an adequate discretization of the poloidal divertor volume. This decomposition is guided by the shape of the unperturbed separatrix according to figure 5 right. An overview of the grid topology is given in figure 9 b. Dark and light blue cell surfaces are connected by a cell surface mapping while periodic boundary conditions are applied for green cell surfaces. Here we use the following grid resolution for each toroidal block:

	n_r	n_p	n_t
Core (A)	48	720	16
SOL (B)	32	864	16
PFR (C)	6	144	16

leading to a total cell number of $N_{\text{cell}} = 3027456$.

5.2. Field line reconstruction

The $n = 3$ RMP field at DIII-D introduces an open chaotic system in the plasma edge in a similar way as in

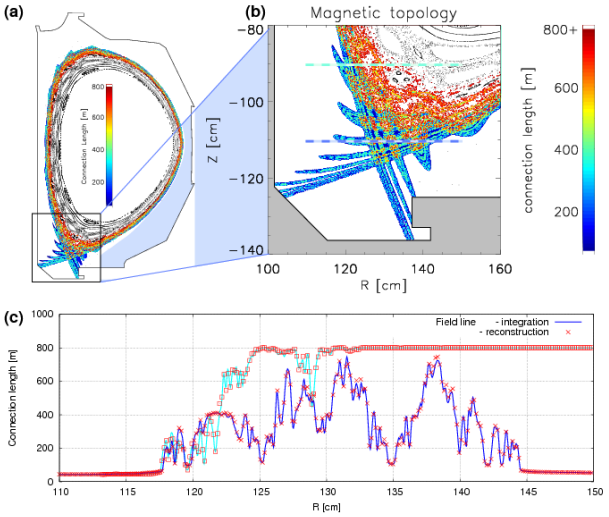

Figure 10: (a,b) 2D cuts of the connection length L_c of magnetic field lines and (b) radial profiles at $Z_1 = -90$ cm and $Z_2 = -110$ cm comparing the reconstructed L_c to the original L_c from field line integration.

TEXTOR tokamak. The magnetic field structure is depicted in figure 10.a,b by 2D cuts of the wall-to-wall connection length L_c of magnetic field lines. It is shown that the reconstructed field structure is in good agreement with the original one obtained from direct field line integration (figure 10.c).

5.3. Transport verification

Now we want to verify the correct treatment of plasma transport in a poloidal divertor configuration. For this we examine an axisymmetric magnetic configuration, i.e. a configuration without RMP field, with a known semi-analytic solution. In this case a separatrix exists (remember figure 1) with closed magnetic surfaces inside. Plasma parameters are constant on these flux surfaces due to the fast parallel transport (e.g. T_e in figure 11). Hence, the normalized poloidal magnetic flux ψ^* can be used as radial coordinate so that $n_e = n_e(\psi^*)$ and $T_e = T_e(\psi^*)$. For a preset constant plasma background the 3D transport equations then reduce to a 1D balance inside the separatrix ($\psi^* \leq 1$), e.g. for the electron temperature:

$$\frac{\partial T_e}{\partial \psi^*} = -\frac{P_{\text{in,e}}}{A^*_\psi \, \overline{|\nabla \psi^*|} \, n_e \, \chi_\perp}. \tag{32}$$

The total input power for electrons $P_{\text{in,e}}$, the electron density n_e and the cross-field diffusion coefficient $\chi_\perp$ are set to the following values for our test case:

$P_{\text{in,e}}$	$= 3.2\,\text{MW}$
n_e	$= 2 \cdot 10^{19}\,\text{m}^{-3}$
$\chi_\perp$	$= 1.2\,\text{m}^2\,\text{s}^{-1}$

while the area A_{ψ^*} of flux surface ψ^* is determined by the given magnetic configuration as well as the flux surface averaged gradient

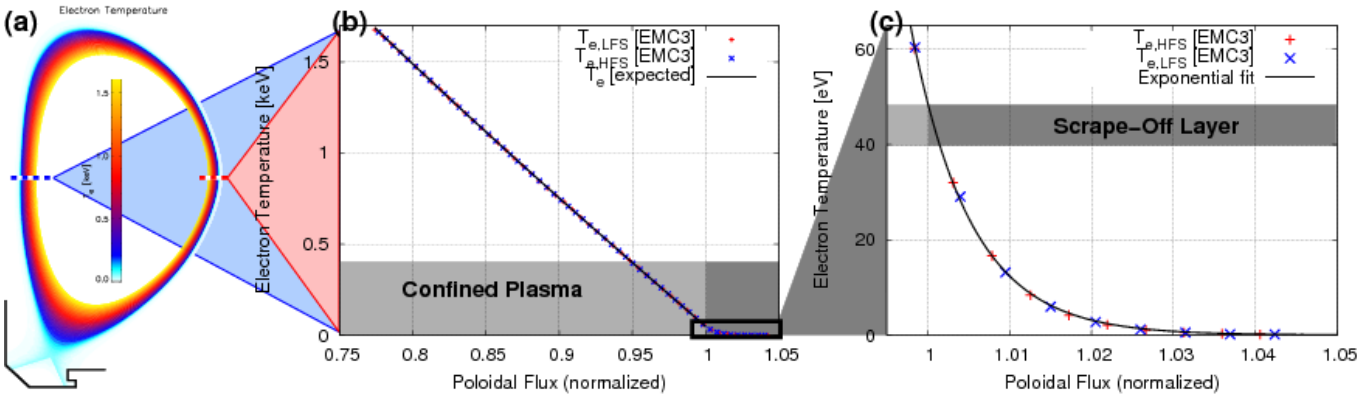

Figure 11: (a) 2D cut of the electron temperature T_e at $\varphi = 0$ deg and (b,c) radial T_e profiles extracted at the inner (High Field Side, HFS) and outer (Low Field Side, LFS) midplane.

$$A_{\psi^*}\overline{|\nabla\psi^*|} \;=\; \oint_{A_{\psi^*}} dA\,\mathbf{e}_{\psi^*}\cdot\nabla\psi^*. \tag{33}$$

Outside the separatrix ($\psi^* > 1$), in the so called *Scrape-Off Layer* (SOL), exponential decay

$$T_e(\psi^*) \;=\; T_{e,\mathrm{LCFS}}\,\exp\left[-\frac{\psi^*-1}{\lambda^*_{T_e}}\right], \tag{34}$$

with an e-folding length $\lambda^*_{T_e}$ is expected, because of parallel losses, i.e. the sink action in parallel direction due to free streaming along $\mathbf{B}$ and plasma recombination at divertor targets. Exponential decay is recoverd very accurately with the EMC3-code (see figure 11.c):

$$T_{e,\mathrm{LCFS}} \;=\; (48.7\pm0.2)\ \mathrm{eV} \tag{35}$$

$$\lambda^*_{T_e} \;=\; (7.32\pm0.05)\ \cdot\ 10^{-3} \tag{36}$$

$\lambda^*_{T_e}$ is an e-foldling length with respect to ψ^*, but it can be related to an average e-folding length in real space:

$$\lambda_{T_e} \;=\; \lambda^*_{T_e}\cdot\overline{|\nabla\psi^*|}^{-1}_{\mathrm{LCFS}} \;=\; (3.35\pm0.02)\ \mathrm{mm} \tag{37}$$

where $\overline{|\nabla\psi^*|}_{\mathrm{LCFS}}$ is the average gradient of the normalized poloidal flux ψ^* at the separatrix. An analytic estimate for λ_{T_e} from a corresponding flux balance is given in [37] which reduces for constant n_e to

$$\lambda_{T_e} \;=\; \sqrt{\frac{\chi_\perp\, L_{\mathrm{core}}}{2\,\gamma_e\, c_s}} \;=\; 3.2\,\mathrm{mm} \tag{38}$$

with sheath heat-transmission factor γ_e and ion sound speed c_s. L_{core} is the length where SOL field lines are in contact with the confined plasma. This estimate is within 5 % of the calculated value, which is a good agreement regarding the very crude approximation made here. Using $T_{e,\mathrm{LCFS}}$ from (35), T_e can be integrated from the separatrix inwards using (32). Figure 11.b shows that the EMC3 data very accurately fits this prediction. T_e at the inner simulation boundary is predicted to $T_e = 1.68\,\mathrm{keV}$, while T_e from EMC3 is $T_e = 1.67\,\mathrm{keV}$, computed on 32 CPUs with 1000 Monte Carlo particles each.

5.4. Convergence of simulation runs

Self-consistent simulations of edge plasma transport require an iterative application of the transport solver described in section 2. As measure for the convergence of simulations runs, the relative change $\Delta\mathcal{F}$ between iterations is taken:

$$\Delta\mathcal{F}^{(n)}[\%] \;=\; \frac{\sum_i \left|\mathcal{F}_i^{(n-1)} - \mathcal{F}_i^{(n)}\right| C_i}{\sum_i \left(\mathcal{F}_i^{(n-1)} + \mathcal{F}_i^{(n)}\right) C_i} \;\times\; 100. \tag{39}$$

To account for strong non-linearities in e.g. the heat conductivity ($\kappa \sim T^{5/2}$), we apply a relaxation scheme

$$\mathcal{F}_j^{(n,\mathrm{relax})} \;=\; \alpha_{\mathrm{relax}}\,\mathcal{F}_j^{(n-1)} \;+\; (1-\alpha_{\mathrm{relax}})\,\mathcal{F}_j^{(n)}, \tag{40}$$

where we have chosen $\alpha_{\mathrm{relax}} = 0.3$ for density and momentum iterations and $\alpha_{\mathrm{relax}} = 0.5$ for energy iterations. An example of a self-consistent solution for the electron temperature is shown in fig. 12. Calculations were started with 1000 MC particles per CPU on 32 CPUs in total and after 15 iterations the number of MC particles was increased to 10k per CPU (figure 13). Then the relative changes Δn_e, ΔT_e, ΔT_i are reduced to a level below 3 % and stay on that level. After another 12 iterations the level of relative changes is further reduced to below 1 % by increasing the number of MC particles (here by increasing the number of CPUs to 256). About 8400 CPUh were used for the entire simulation on an IBM Power6 575 System at Rechenzentrum Garching. Discussion of numerical results will be published as subsequent work.

6. Summary and Conclusions

A Lagrangian scheme for 3D edge plasma transport simulations is described which is implemented in the EMC3-EIRENE code. The code utilizes a field aligned grid for

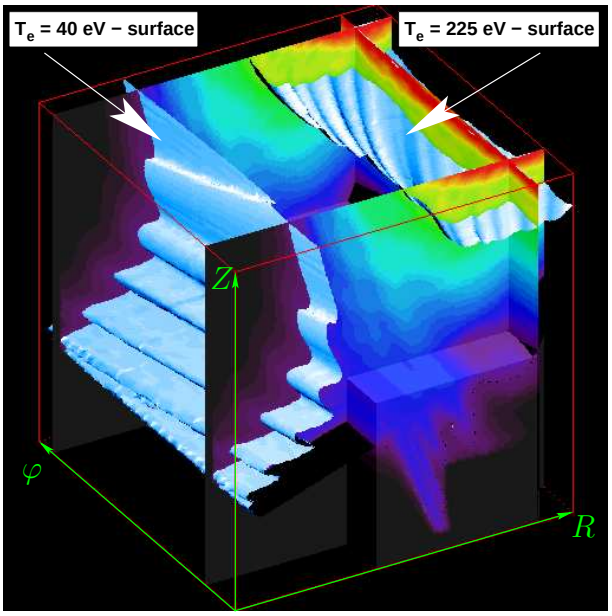

Figure 12: Self-consistent solution of the 3D electron temperature T_e in the X-point region (compare figure 10.b): $R = 100 \ldots 160\,\mathrm{cm}$, $Z = -140 \ldots -80\,\mathrm{cm}$, $\varphi = -20 \ldots 100$ deg. Blue shaded surfaces indicate $T_e = \mathrm{const}$ surfaces.

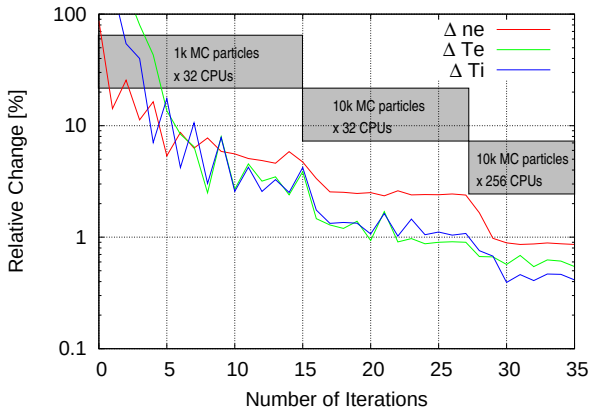

Figure 13: Convergence of a simulation run with the EMC3-EIRENE code. The calculations were started with 1000 MC particles on 32 CPUs each. After 15 iterations the number of MC particles was increased to 10k per CPU and after another 12 iterations the number of CPUs was increased to 256.

fast reconstruction of magnetic field lines. This technique has been generalized to unstructured - but in practise still block-structured - grids in order to allow simulations for fusion devices with complex shape of the edge plasma region. The correct performance of the generalized code was demonstrated by numerical tests and comparisons to reduced transport models. These tests document the enhanced applicability of the EMC3-EIRENE code for present fusion devices, in particular for tokamaks with poloidal divertor. This allows for the first time 3D self-consistent calculations of particle, parallel momentum and energy transport as well as kinetic recycling neutrals for ITER relevant plasma scenarios.

Appendix

A. Plasma transport equations

The EMC3-EIRENE code solves a time-independent set of plasma transport equations for density n_e, parallel momentum $u_{i\parallel}$ and electron and ion temperature T_e and T_i, respectively:

- Particle balance:

$$\nabla \cdot \left(\mathbf{e}_\parallel \, n_i \, u_{i\parallel} \; - \; \underline{\mathbf{I}}_\perp \cdot D_\perp \nabla \, n_i \right) \; = \; S_p \qquad (41)$$

- Momentum balance:

$$\begin{aligned} & \nabla \cdot \mathbf{e}_\parallel \left[m_i \, n_i \, u_{i\parallel}^2 \; - \; \eta_\parallel \, \mathbf{e}_\parallel \cdot \nabla \, u_{i\parallel} \right] \\ & - \nabla \cdot \underline{\mathbf{I}}_\perp \cdot D_\perp \, \nabla \, m_i \, n_i \, u_{i\parallel} \\ & = - \, \mathbf{e}_\parallel \cdot \nabla \, n_i \; (T_i \; + \; T_e) \; + \; S_m \end{aligned} \qquad (42)$$

- Energy balance ions:

$$\begin{aligned} & \nabla \cdot \mathbf{e}_\parallel \left[\frac{5}{2} \, n_i \, T_i \, u_{i\parallel} \; - \; \kappa_{i\parallel} \, \mathbf{e}_\parallel \cdot \nabla \, T_i \right] \\ & - \nabla \cdot \underline{\mathbf{I}}_\perp \cdot \left[\frac{5}{2} \, T_i \, D_\perp \, \nabla \, n_i \; + \; \chi_{i\perp} \, n_i \, \nabla \, T_i \right] \\ & = - \; k \; (T_i \; - \; T_e) \; + \; S_{ei} \end{aligned} \qquad (43)$$

- Energy balance electrons:

$$\begin{aligned} & \nabla \cdot \mathbf{e}_\parallel \left[\frac{5}{2} \, n_i \, T_e \, u_{i\parallel} \; - \; \kappa_{e\parallel} \, \mathbf{e}_\parallel \cdot \nabla \, T_e \right] \\ & - \nabla \cdot \underline{\mathbf{I}}_\perp \cdot \left[\frac{5}{2} \, T_e \, D_\perp \, \nabla \, n_i \; + \; \chi_{e\perp} \, n_i \, \nabla \, T_e \right] \\ & = k \; (T_i \; - \; T_e) \; + \; S_{ee} \end{aligned} \qquad (44)$$

where $\mathbf{e}_\parallel$ is the unit vector along magnetic field lines, $\underline{\mathbf{I}}_\perp = \underline{\underline{I}} - \mathbf{e}_\parallel \, \mathbf{e}_\parallel$ with $\underline{\underline{I}}$ beeing the unit tensor, n_i the ion and electron density, $u_{i\parallel}$ the parallel ion velocity, T_e and T_i the electron and ion temperatures, respectively, $D_\perp$, $\chi_{e\perp}$,

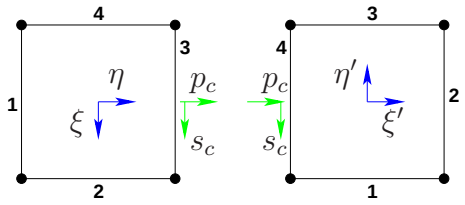

Figure 14: Orientation of local coordinate system, i.e. cell surfaces i_{surf}, i'_{surf} between adjacent cells. Example: $\eta = 1$ - surface ($i_{\text{surf}} = 3$) meets $\xi' = -1$ - surface ($i'_{\text{surf}} = 4$).

$\chi_{i\perp}$ anomalous cross-field transport coefficients for particles, electron and ion energy, $\eta_{\parallel}$ the parallel ion viscosity, $\kappa_{e\parallel}$, $\kappa_{i\parallel}$ parallel electron and ion heat conductivity and S_p, S_m, S_{ei}, S_{ee} sources due to interaction with neutral particles.

B. Coordinate transformation

The transformation of local coordinates (ξ, η) at the cell boundary can be written in the compact form:

$$(\xi', \eta') = \mathbf{M}_{\xi\eta} \cdot (\xi, \eta). \tag{45}$$

where $\mathbf{M}_{\xi\eta}$ depends on the relative orientation of the local coordinate systems, i.e. the surface numbers i_{surf}, i'_{surf} (figure 14). In any case there is a surface coordinate s_c which is fixed and a perpendicular coordinate p_c which is transformed to $-p_c$. Depending on the orientation i_{surf} the coordinates (s_c, p_c) are

$$\begin{pmatrix} s_c \\ p_c \end{pmatrix} = \mathbf{A}_{i_{\text{surf}}} \begin{pmatrix} \xi \\ \eta \end{pmatrix} \tag{46}$$

and depending on the orientation i'_{surf} the new coordinates (ξ', η') are

$$\begin{pmatrix} \xi' \\ \eta' \end{pmatrix} = \mathbf{B}_{i'_{\text{surf}}} \begin{pmatrix} s_c \\ -p_c \end{pmatrix}. \tag{47}$$

Basically $\mathbf{A}$ and $\mathbf{B}$ are rotations

$$\mathbf{R}(\varphi) = \begin{pmatrix} \cos\varphi & \sin\varphi \\ -\sin\varphi & \cos\varphi \end{pmatrix} \tag{48}$$

of the coordinate system with angles

$$\varphi_A = (i_{\text{surf}} - 3) \cdot \frac{\pi}{2} \tag{49}$$

$$\varphi_B = (-i'_{\text{surf}} + 1) \cdot \frac{\pi}{2}. \tag{50}$$

(46) and (47) can be combined to determine the transformation matrix $\mathbf{M}_{\xi\eta}$:

$$\mathbf{M}_{\xi\eta} = \mathbf{B}_{i'_{\text{surf}}} \begin{pmatrix} 1 & 0 \\ 0 & -1 \end{pmatrix} \mathbf{A}_{i_{\text{surf}}}. \tag{51}$$

Inserting (48) gives

$$\mathbf{M}_{\xi\eta} = \begin{pmatrix} \cos(\varphi_A - \varphi_B) & \sin(\varphi_A - \varphi_B) \\ \sin(\varphi_A - \varphi_B) & -\cos(\varphi_A - \varphi_B) \end{pmatrix} \tag{52}$$

and (49), (50) and $m = i_{\text{surf}} + i'_{\text{surf}}$ gives

$$\mathbf{M}_{\xi\eta} = \begin{cases} (-1)^{\frac{m}{2}} \cdot \mathbf{M}_0, & m \text{ even} \\ (-1)^{\frac{m-1}{2}} \cdot \mathbf{M}_1, & m \text{ odd} \end{cases} \tag{53}$$

with $\mathbf{M}_0$, $\mathbf{M}_1$ from (30).

References

[1] B. Kadomtsev. *Tokamak Plasma; A Complex Physical System.* Institute of Physics Publishing, Bristol and Philadelphia, 1992.
[2] J. Wesson. *Tokamaks.* Oxford: Clarendon Press, 2004.
[3] D. Reiter. *Journal of Nuclear Materials*, 196-198:80–89, 1992.
[4] D. Reiter et al. *Fusion Science and Technology*, 47:172, 2005.
[5] R. Schneider et al. *Contrib. Plasma Phys.*, 46(1-2):3–191, 2006.
[6] A. Taroni et al. *Contrib. Plasma Phys.*, 32(3-4):438–443, 1992.
[7] R. Simonini et al. *Contrib. Plasma Phys.*, 34(2-3):368–373, 1994.
[8] H. Kawashima et al. *Plasma Fusion Res.*, 1:31, 2006.
[9] H. Kawashima et al. *Fusion Engineering and Design*, 83:1643–1647, 2008.
[10] L. Spitzer. *Phys. Fluids*, 1:253, 1958.
[11] Y. Feng et al. *Journal of Nuclear Materials*, 241-243:930–934, 1997.
[12] Y. Feng et al. *Journal of Nuclear Materials*, 266-269:812–818, 1999.
[13] Y. Feng et al. *27th EPS Conference on Contr. Fusion and Plasma Phys.*, volume 24B, pages 1188–1191, Budapest, 12-16 June 2000.
[14] M. Kobayashi et al. *Contrib. Plasma Phys.*, 44(1-3):25–30, 2004.
[15] M. Kobayashi et al. *Nuclear Fusion*, 44:S64–S73, 2004.
[16] D. Harting et al. *Contrib. Plasma Phys.*, 48(1-3):1–7, 2008.
[17] M. Kobayashi et al. *Nuclear Fusion*, 47:61–73, 2007.
[18] Y. Feng et al. *Plasma Phys. Control. Fusion*, 44:611–625, 2002.
[19] Y. Feng et al. *Contrib. Plasma Phys.*, 44(1-3):57–69, 2004.
[20] D. Sharma et al. *Nuclear Fusion*, 45:825–836, 2005.
[21] M. Kobayashi et al. *Journal of Nuclear Materials*, 363-365:294–300, 2007.
[22] Y. Feng et al. *Nuclear Fusion*, 48:024012, 2008.
[23] Y. Feng et al. *Phys. Plasmas*, 12(052505):1–7, 2005.
[24] H. Zohm. *Plasma Phys. Control. Fusion*, 38:105–128, 1996.
[25] T.E. Evans et al. *Phys. Rev. Lett.*, 92(23):(235003), 2004.
[26] S.I. Braginskii. *Review of Plasma Physics*, 1:205–311, 1965.
[27] P.E. Kloeden and E. Platen. *Numerical solution of Stochastic Differential Equations.* Springer-Verlag, 1999.
[28] J.-P. Minier et al. *Physics Reports*, 352:1–214, 2001.
[29] G. Maruyama. *Rend. Circ. Mat. Palermo*, 4:48–93, 1955.
[30] H. Risken. *The Fokker-Planck equation.* Springer-Verlag, Berlin, 2nd edition, 1989.
[31] T. J. R. Hughes. *The Finite element method : linear static and dynamic finite element analysis.* Prentice-Hall, 1987.
[32] A.M. Runov et al. *Phys. Plasmas*, 8(3):916–930, 2001.
[33] K.H. Finken et al. *Nuclear Fusion*, 39(5):637–662, 1999.
[34] S.S. Abdullaev et al. *Phys. Plasmas*, 8(6):2739–2749, 2001.
[35] O. Schmitz et al. *Nuclear Fusion*, 48:024009, 2008.
[36] L.L. Lao et al. *Nuclear Fusion*, 25:1611–1622, 1985.
[37] P.C. Stangeby. *The Plasma Boundary of Magnetic Fusion Devices.* Institute of Physics Publishing Bristol and Philadelphia, 2000.